Journal of Materials Chemistry A

ROYAL SOCIETY OF CHEMISTRY

PAPER

View Article Online
View Journal | View Issue

Check for updates

Cite this: J. Mater. Chem. A, 2025, 13, 14335

A polymeric mixed conductor-based solid state charge storage device†

Prem D. Nayak, [a] David Ohayon, [a] Luca Salvigni,[a] Sumana Bhattacharjee,[a] Danilo Arcangeli,[a] Tania Cecilia Hidalgo Castillo, [a] Adel Hama, [a] Johana Uribe,[a] Rajendar Sheelamanthula,[b] Haoran Tang, [c] Iain McCulloch,[bd] Fei Huang [c] and Sahika Inal *[a]

Organic mixed ionic and electronic conductors (OMIECs) are soft materials capable of reversibly storing electronic charges in their bulk, stabilized by ionic charges typically introduced from an electrolyte. Recent advancements in OMIEC design have improved their ion uptake and transport properties, increasing the number of charges stored per monomer unit, thus making them attractive candidates for charge storage devices. However, the use of aqueous electrolytes, common in OMIEC based systems, limit storage performance due to their narrow voltage window. In this work, we introduce an OMIEC-based charge storage device that operates with an ionic liquid gel electrolyte serving as a transparent, solid-state ion reservoir within a full-cell package. This design allows stable operation up to 2.4 V and integrates an embedded failure diagnostics system. To address the critical issue of self-discharge, we incorporated an O_2 and H_2O barrier into the device, significantly improving its performance under ambient conditions. This cell design enables standardized conditions for screening OMIECs, eliminating interference from parasitic reactions or electrolyte instability. Using this system, we systematically evaluated a range of n-type OMIECs and identified the optimal anode material. The resulting device demonstrated a capacity of ~25 mA h g^{-1} and an energy density of ~118 W h kg^{-1}, surpassing the performance of existing OMIEC-based systems. This work represents a step toward safer and more efficient polymer-based charge storage technologies.

Received 5th November 2024
Accepted 1st March 2025

DOI: 10.1039/d4ta07873j

rsc.li/materials-a

Introduction

The global shift towards renewable energy and low carbon footprint technologies, along with the increasing demand for portable and wearable electronic devices, calls for diverse and efficient charge storage solutions. While much of the research has focused on increasingancing capacity, charging speed and form factor versatillity, materials selection should also prioritize safety, environmental sustainability, and ethical standards. Conjugated polymer offer a promising path forward, as they are composed of earth-abundant elements and exhibit high solubility in solvents commonly used for recycling.[1–5] Their solution processability supports scalable, large-area manufacturing without the need for high temperature processing, and their synthetic tunability allows for the customization of electrochemical properties to meet specific application requirements.[6,7]

A unique subset of conjugated polymers includes organic mixed ionic-electronic conductors (OMIECs), semiconductors that naturally interact with electrolytes, serving as sources of ionic charges. The presence of ion-transporting side chains in some OMIECs enables electronic charge stabilization by counterions throughout their bulk, allowing for volumetric charge storage.[8,9] Depending on the side chain chemistry, both hydrated and relatively hydrophobic ions can penetrate the film and couple with the electronic charges.[10] Through a combination of electrochemical and electrostatic doping at low temperatures, it is even possible to fully deplete the valence band and access deeper energy levels, leading to charge carrier densities that surpass those attainable by conventional chemical doping methods.[11] While side chain engineering allows for control over ion transport, the choice of the conjugated backbone dictates the electronic transport type, hole (p-type) electron (n-type), or ambipolar, allowing OMIECs to function as

[a]Organic Bioelectronics Laboratory, Biological and Environmental Science and Engineering Division, King Abdullah University of Science and Technology (KAUST), Thuwal 23955-6900, Saudi Arabia. E-mail: sahika.inal@kaust.edu.sa

[b]KAUST Solar Center, Physical Sciences and Engineering Division, KAUST, Thuwal 23955-6900, Saudi Arabia

[c]Institute of Polymer Optoelectronic Materials and Devices, State Key Laboratory of Luminescent Materials and Devices, Guangdong Basic Research Center of Excellence for Energy & Information Polymer Materials, South China University of Technology (SCUT), Guangzhou, China

[d]Department of Chemistry, Chemistry Research Laboratory, University of Oxford, Oxford OX1 3TA, UK

† Electronic supplementary information (ESI) available. See DOI: https://doi.org/10.1039/d4ta07873j

both anodes and cathodes in fully organic devices.[12] Their ability to readily uptake ions supports high charge–discharge speeds and enables low-voltage operation for both oxidation and reduction processes in p-type and n-type materials, respectively.[13] Furthermore, OMIECs generally exhibit good biocompatibility and tunable mechanical properties, making them well suited for the fabrication of flexible devices capable of directly interfacing with living tissue.[14–16] This unique combination of properties makes OMIECs particularly attractive for next-generation charge storage devices—particularly those requiring unconventional form factors or direct integration with *in vivo* bioelectronics.

Among the key components of an electrochemical charge storage device, the electrolyte plays an important role by providing ionic connection between the electrodes and supplying the ions necessary for doping OMIEC electrodes. The few reported OMIEC-based charge storage devices rely on either aqueous[1,13] or organic electrolytes.[17] While aqueous electrolytes are attractive due to their low cost, safety, and biocompatibility, the resulting cells suffer from a narrow operational voltage window and the high volatility of the electrolytes lead to changes in ion concentration, necessitating frequent refilling.[5] Organic electrolytes, on the other hand, while offering wider voltage windows, raise concerns due to their volatility, flammability, and leakage risks, factors that are particularly problematic for bioelectronics applications. Ionic liquids are a compelling alternative to both aqueous and organic electrolytes. Ionic liquid electrolytes exhibit minimal vapor pressure, outstanding resistance to flammability, and excellent thermal and chemical stability.[18] They enable operation over a broad electrochemical window - beyond the water splitting limit,[19] making deeper doping states in OMIECs accessible. A recent study demonstrated that with ionic liquids, the OMIECs reach higher doping levels at lower overpotentials compared to aqueous electrolytes, resulting in increased gravimetric capacity.[20] Furthermore, ionic liquids can be incorporated into polymer matrices to form solid-state electrolyte gels, which can be molded into various shapes. With established separation processes already in place, ionic liquids are also infinitely recyclable.[21] While OMIEC films have been integrated with ionic liquids, hydrogels, and eutectogels in the context of electrochemical transistors,[22] their performance under charge storage device operating conditions remains largely unexplored.

One major challenge in the development of OMIEC-based charge storage devices is the management of self-discharge - a spontaneous voltage decay that leads to the rapid loss of stored energy. Self-discharge arises from several mechanisms, including charge redistribution, parasitic Faradaic reactions, and ohmic leakage.[23] Among these, parasitic side reactions, such as oxygen reduction reaction (ORR), hydrogen evolution reaction (HER), and oxygen evolution reaction (OER), are the most predominant, and particularly observed in n-type OMIECs.[24–26] Current approaches to mitigate this issue involve degassing liquid-state electrolytes with inert gases or operating the devices in controlled inert environments or sealed architectures.[1,27] While these methods are effective in laboratory-scale, proof-of-concept demonstrations, they often exaggerate the apparent charge storage capabilities and are not suitable for scalable, real-world applications. In practical scenarios, robost encapsulation is necessary to prevent peformance losses.

In this work, we present an OMIEC based charge storage device that incorporates 1-ethyl-3-methylimidazolium bis(trifluoromethylsulfonyl)imide (EMIM-TFSI) in a solid gel electrolyte format. To address the critical challange of Faradaic reaction-driven self discharge, we introduce an O_2/H_2O barrier that significantly enchances the stability of the electrodes. After a comprehensive evaluation of capacity and self-discharge behaviour, we identified the optimal combination of n-type and p-type OMIECs to construct an all OMIEC full cell. The resulting device achieves a potential of 2.4 V and a full-cell capacity of approximately 25 mA h g^{-1}, exceeding the voltage and capacity benchmarks of all previously reported all-OMIEC cells.[1] The performance of this cell is made possible by the integrated O_2/H_2O barrier, which effectively mitigates the often overlooked issue of Faradaic self-discharge. Additionally, the inclusion of a reference electrode enables internal diagnostics, and the cell's optical transparency allows for *in situ* spectroscopy-based probing.

Results and discussion

The design of the OMIEC based cell with the ionic liquid-based gel

In this work, we propose an approach to fabricating a charge storage device that includes, in addition to the cathode (p-type OMIEC) and anode (n-type OMIEC), two additional electrodes: a reference electrode (Ag/AgCl pseudo-reference electrode) and a counter electrode (carbon paper). This setup enables both half- and full-cell evaluations, providing more meaningful information and a more accurate correlation between full-cell data and single-electrode behavior (Fig. 1a). All components are arranged laterally on a glass substrate. The cathode and anode electrodes were fabricated on carbon paper substrates, which were attached to gold electrode contacts using carbon paste. Gold-coated areas not covered by OMIEC materials were insulated with a Parylene-C layer. The electrodes and the solid gel electrolyte were sequentially assembled on a bottom glass slide, which was then encapsulated with another glass slide on top. The gap between the glass slides was filled with an O_2 and H_2O barrier, processed through crosslinking with UV light and heat, respectively, to prevent parasitic discharge. The final device has an active area of 1×1 cm^2 and a typical mass loading of 0.1 mg cm^{-2}, unless mentioned otherwise.

To evaluate performance across material combinations, we screened two p-type OMIECs in combination with four different n-type OMIECs (Fig. 1b). The n-type anodes included P-90[26,28] and p(C_6-NDI-T),[29,30] both based on donor–acceptor type naphthalene diimide-bithiophene (NDI-T2) or thiophene (NDI-T) backbones functionalized with ethylene oxide side chains to enhance wetting with ionic liquids. We also tested a printable n-type ink composed of the side-chain-free n-type mixed conductor, poly(benzimidazobenzophenanthroline) (BBL), dispersed in ethanol (referred to as n-ink).[31] BBL-based films have previously demonstrated suitability as anodes of aqueous-

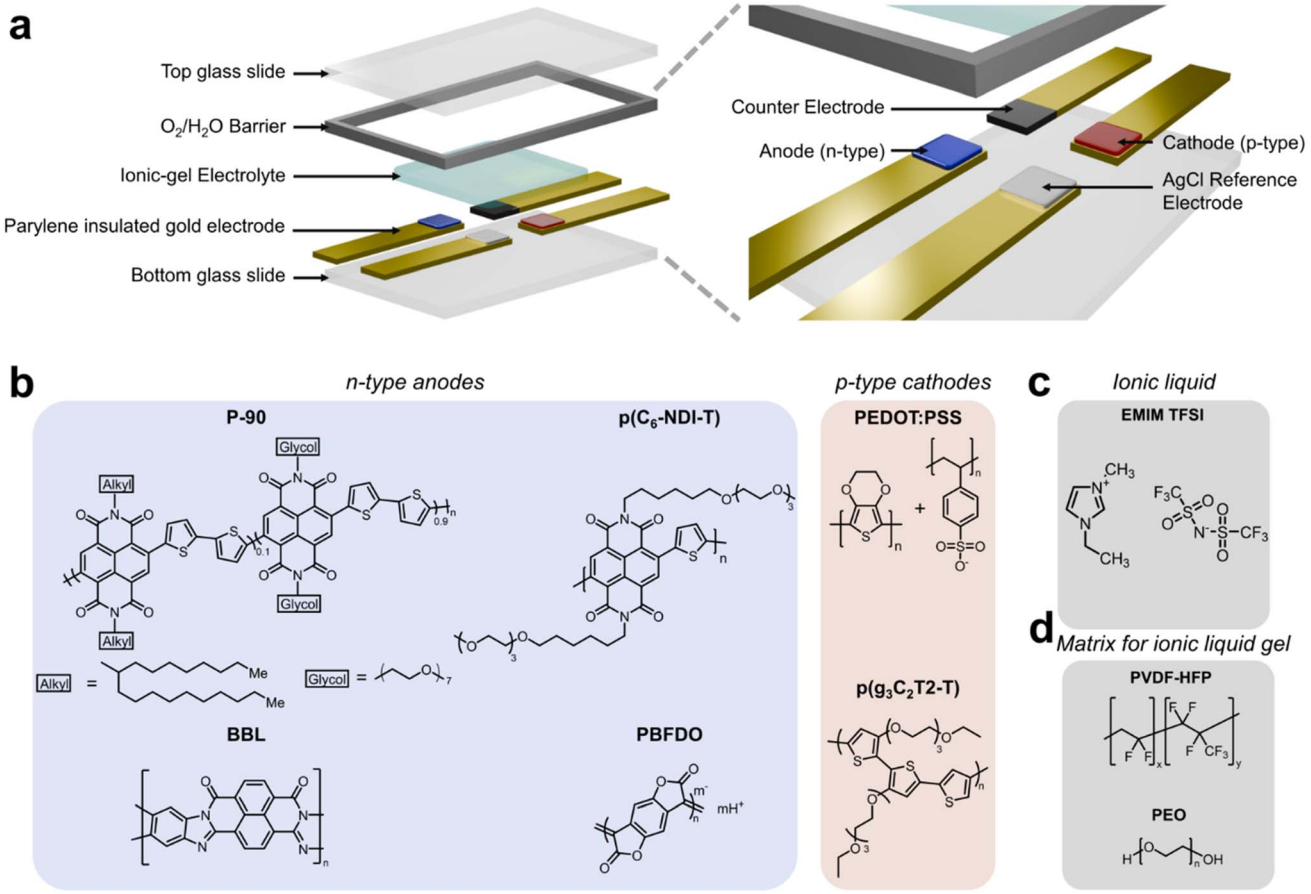

Fig. 1 (a) Schematic of the full-cell design with half-cell testing capability. The active electrode area is 1 cm^2, the electrolyte size is 2.2 × 2.2 cm^2, and the whole device covers an area of 7.5 × 2.5 cm^2. (b) Chemical structures of the n-type and p-type OMIECs used in the study, (c) the ionic liquid 1-ethyl-3-methylimidazolium bis(trifluoromethylsulfonyl)imide (EMIM-TFSI) and (d) the polymers used for the matrix forming the gel: poly(vinylidene fluoride-*co*-hexafluoropropylene) (PVDF-HFP) and polyethylene oxide (PEO).

operating supercapacitors and batteries.[2,32] Finally, on the list of n-type OMIEC tested was poly(benzodifurandione) (PBFDO), recently reported for its high conductivity.[33–35] As cathode materials, we used a thiophene-based mixed conductor, p(g_3C_2T2-T), and the widely used benchmark OMIEC, poly(3,4-ethylenedioxythiophene):polystyrene sulfonate (PEDOT:PSS).[36]

As for the ionic liquid, we chose EMIM-TFSI, a material commonly used in OMIEC-based studies (Fig. 1c).[37–40] To create a fully solid-state device, the ionic liquid is typically embedded within a polymeric matrix, most often poly(-vinylidene fluoride-*co*-hexafluoropropylene) (PVDF-HFP, Fig. 1d), a network-forming polymer commonly used as a dielectric in organic transistors.[18,37,39] Upon solvent evaporation, the composite forms a self-standing solid electrolyte gel. However, the solvent used to prepare the PVDF-HFP gel is acetone, which either dissolves or delaminates OMIEC films underneath, or the film peels off from the surface easily once the solvent evaporates. Additionally, PVDF-HFP gel solution tends to phase-separate if not used immediately, requiring reheating and reprocessing to restore homogeneity (Fig. S1†). These drawbacks hinder long-term intimate contact between the electrolyte and active material, which is crucial for efficient charging, making PVDF-HFP a suboptimal polymer matrix choice. To overcome these limitations, we replaced PVDF-HFP with high molecular weight polyethylene oxide (PEO, Fig. 1d). PEO dissolved in acetonitrile forms a stable, transport, and uniform gel for the IL encapsulation, with a shelf lifetime exceeding 30 days (Fig. S1†). The resulting films exhibit strong adhesion to OMIEC surfaces and improved process reliability (Fig. S2†).

Fig. 2a–f demonstrate the cyclic voltammograms of our OMIEC films recorded in both the PEO-based gel electrolyte and an aqueous 0.1 M NaCl solution, using the lateral reference and counter electrodes of our cell. All polymer films show a combination of redox peaks and capacitive charging behavior within a similiar electrochemical window in both electrolytes. Importantly, the carbon electrode shows negligible capacitance (Fig. S3†), ensuring that the recorded signals reflect the intrinsic properties of the OMIEC films while PEDOT:PSS, P-90, and p(C_6-NDI-T) exhibit similar CV profiles in both electrolytes, p(g_3C_2T2-T) and PBFDO display a more pronounced capacitive behavior in the ionic liquid compared to the aqueous electrolyte (Fig. 2f, Table S1†).BBL, however, shows a reduced capacitive response in the gel relative to 0.1 M NaCl, potentially due to poor wetting.

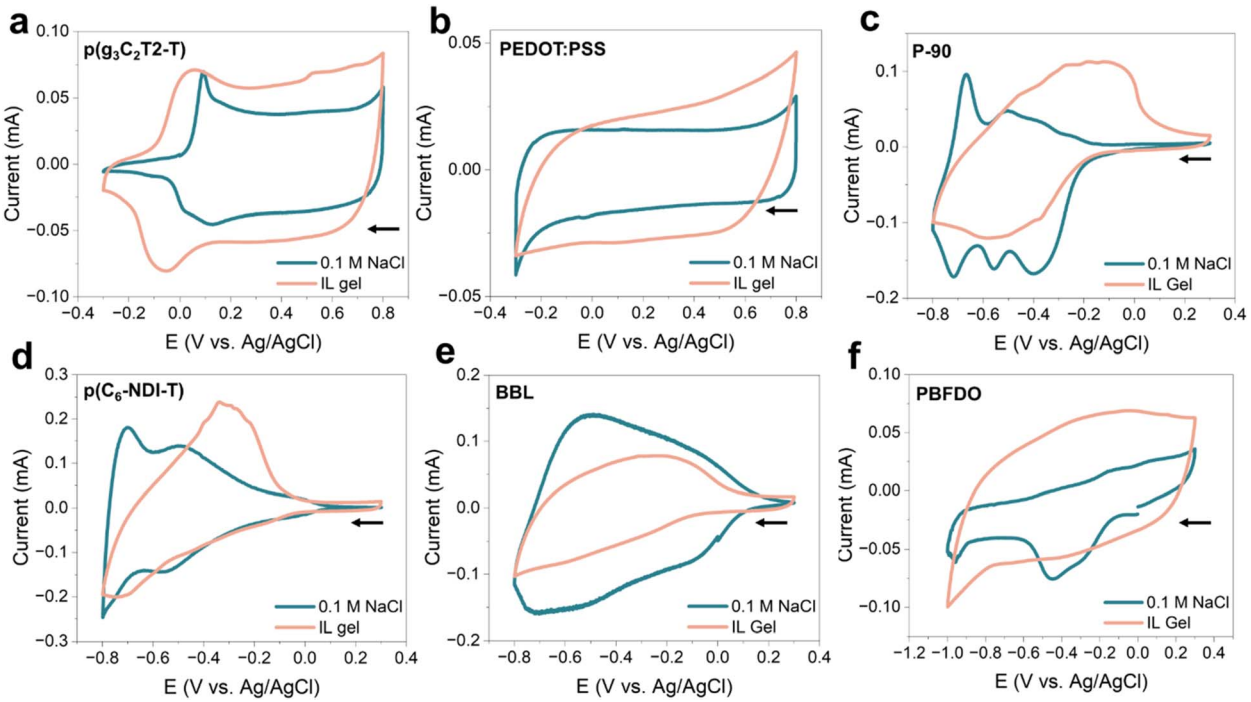

Fig. 2 Cyclic voltammograms (2nd cycle) of OMIEC electrodes in 0.1 M NaCl electrolyte and the ionic liquid gel: (a) p(g_3C_2T2-T), (b) PEDOT:PSS, (c) P-90, (d) p(C_6-NDI-T), (e) BBL and (f) PBFDO. Scan rates were 5 mV s^{-1} for all the measurements. Measurements with IL gel were done in an N_2 filled glove box environment and the CVs with 0.1 M NaCl were tested in a N_2 bubbled electrolyte in ambient environment. Arrows indicate the scan direction. Measurements were performed with two different electrodes with the same mass loading.

These results confirm that ionic liquid gels are viable electrolytes for reversible doping of OMIEC materials. While BBL exhibits lower capacitance in the gel, the other materials show comparable or even superior capacitance relative to aquoues conditions. Understanding these electrochemical differences between aqueous and gel-based electrolytes requires a multi-parametric evaluation that accounts for factors such as ion size, dissociation constants, ionic charge density and the complex microstructure and wetting behaviour of the OMIEC films.[41]

Fig. S4† demonstrates the charging of OMIEC films in the ionic gel up to ±1.2 V *vs.* Ag/AgCl, highlighting the broad operational range enabled by the EMIM:TFSI- based ionic liquid gel, which remains electrochemically stable between +2 V and −2 V *vs.* Ag/AgCl.[19] In contrast, when representative OMIECs, p(g_3C_2T2-T) and PBFDO, are operated in 0.1 M NaCl, significant Faradaic activity emerges beyond ±0.8 V *vs.* Ag/AgCl. As shown in Fig. S5†, operation in the aqueous electrolyte results in bubble formation on the p(g_3C_2T2-T) cathode and delamination of the PBFDO anode - phenomena associated with gas evolution and material instability, which are not observed in the ionic liquid gel.

A particular advantage of the PEO-based gel is its optical transparency, which enables *in operando* optical spectroscopy tests of the OMIEC films during their electrochemical cycling. Fig. S6a† presents the setup used to record the UV-vis spectra of OMIEC films under applied biased in the PEO-based ionic liquid. Fig. S6b and c† demonstrates that the ionic liquid gel facilitates access to the full electrochemical doping range of p(C_6-NDI-T) and p(g_3C_2T2-T) up to *ca.* |1.0| V *vs.* AgCl, revealing the evolution of spectral features associated with neutral and charged states (polarons and bipolarons). These results are consistent with previous findings for the same OMIECs in aqueous electrolytes,[20,42] highlighting that ionic liquid gels can support similar doping behavior while additionally enabling access to deeper charged state access.[20]

The effect of encapsulation on device performance

Upon charging, the electrochemical potentials of the cathode and anode can exceed thresholds that tirgger Faradaic reactions with water and O_2, resulting in side-reactions such as the oxygen reduction reaction (ORR), hydrogen evolution reaction (HER), or oxygen evolution reaction (OER). These reactions can deplete the charged states, leading to self-discharge and a loss in voltage, which consequently diminishes the energy and power output, thereby reducing the overall efficiency of charge storage devices. Therefore, the ingress of O_2 and water into a cell critically impairs device performance. To evaluate the impact of air exposure on these polymeric electrodes, we monitored the half-cell voltage of a representative n-type OMIEC, p(C_6-NDI-T), subsequent to its transition to the doped state. Fig. 3a shows that the film charged to −1.2 V loses the charged state in air as soon as the voltage source is removed. The discharge is rapid and drastic, accounting for 0.95 V (~80% loss). When the same film is charged in an N_2-filled glove box, the discharge is significantly lower, about 23%. The self-discharge behavior in

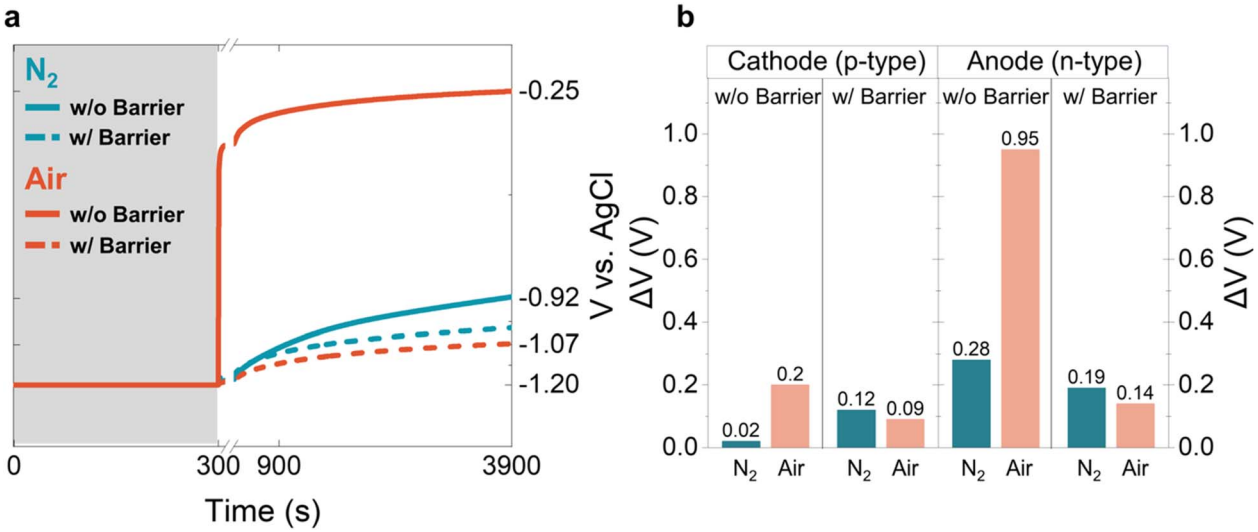

Fig. 3 (a) The evolution of the open circuit potential of p(C_6-NDI-T)-based anode after being charged to −1.2 V *vs.* Ag/AgCl in a N_2-filled glove box and air conditions, without and with the use of a barrier. (b) The change in the open circuit potential of p-type p(g_3C_2T2-T) and n-type p(C_6-NDI-T) films one hour after they films were charged at 1.2 V and −1.2 V *vs.* AgCl, respectively. Measurements were done in oxygen-free and in air in the absence and presence of a barrier. The values shown are the values of potential change.

air not unique to this polymer; all tested n-type OMIEC-based anodes exhibited similar behavior, sugggesting that ORR is the dominant parasitic mechanism and that these materials lack inherent electrocatalytic resistance to suppress it (Fig. S7a†). The p-type material p(g_3C_2T2-T) also shows voltage loss upon air exposure although the effect is less pronounced compared to the n-type films (Fig. S7b†). This loss may be attributed to OER, which leads to electron gain and voltage decay. However, due to the relatively high overpotential (in absolute terms) required for OER, the impact on p-type films is low, resulting in a more stable performance under ambient conditions.

Although our cell's electrolyte is a solid gel, it is based on EMIM TFSI, an ionic liquid capable of dissolving O_2 and H_2O even when trapped in a polymer matrix.[43–45] We, therefore, sealed the device with a glass layer bonded to the bottom layer using an O_2 and H_2O barrier. Fig. 3a illustrates how the barrier inhibits self-discharge in n-type films. In the presence of the barrier, the voltage loss after one hour is reduced to just 140 mV (11.6%), compared to a 950 mV (∼80%) loss in air without the barrier (Fig. 3b). The barrier also improves voltage retention in the p-type film, likely by inhibiting OER processes- the voltage change is reduced from 0.2 V to 0.09 V. The self-discharge behavior for the rest of the n-OMIECs without the barrier is presented in Fig. S7a.†

Notably, even in a nitrogen-filled glovebox with oxygen levels below 1 ppm, n-type OMIECs still exhibited measurable voltage decay, suggesting an intrinsic, non-Faradaic self-discharge mechanism. This is likely thermally driven and attributed to ion decoupling from the polymer backbone.[46] To investigate this, we performed a temperature-dependent study, observing non-Faradaic self-discharge when the device was heated to 373 K. Upon cooling, the discharge rate partially recovered (Fig. S8†); however, the retention voltage did not fully return to its original value, suggesting that elevated temperatures might induce permanent structural rearrangements of the chains.

The OMIEC selection for the top-performing device

OMIECs are typically evaluated as half-cell configurations before being integrated into a full cell with an optimized cathode–anode pair. As illustrated in Fig. 1a, we designed a full cell architecture that supports both full- and half-cell testing, while enabling electrode diagnostics using the pseudo reference electrode (AgCl) (see ESI section 1†). Our goal was to systematically identify the best-performing n-type and p-type OMIECs, not only to present the highest-performing material combination, but also to demonstrate a rigorous screening approach. Each half-cell was first charged to a target potential, follwoed by a 10 minute open circuit period during which self-discharge was monitored. Using a chronopotentiometric method at a constant current of 0.1 A g^{-1}, we incrementally increased the charging potential from −0.3 V to −1.2 V for n-type OMIECs, and from 0.3 V to 1.2 V for p-types. We quantified self-discharge as the percentage of voltage lost after 10 minutes, relative to the final charged voltage (*e.g.*, for a 0.6 V charge, the loss was calculated as the percentage drop from 0.6 V after the rest period). This method allows us to determine which material retains the most voltage and the best charging voltage.

Fig. 4a shows that PBFDO retains ∼90% of its charged voltage, as does p(g_3C_2T2-T), across the full range of applied biases. In contrast, p(C_6-NDI-T) and P-90 exhibit ∼10% voltage losses up to −0.6 V, with a drastic drop when charged to voltages beyond this point. BBL, on the other hand, shows poor retention, with voltage losses a exceeding 10% even at low charging voltages. PEDOT:PSS demonstrates better stability at high oxidation states but suffers from substraintal voltage loss when dedoped. Consequently, among all tested materials,

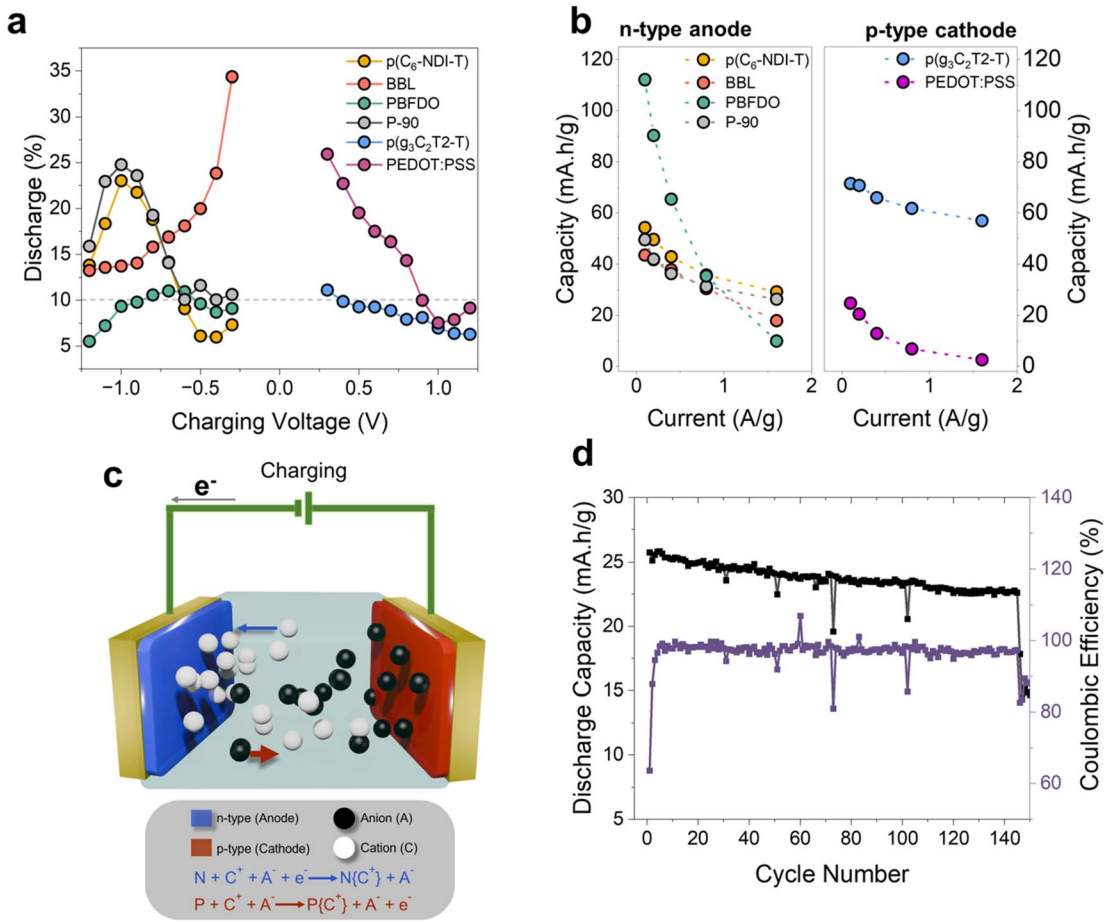

Fig. 4 (a) The voltage drop with respect to charging voltage measured at each contact 10 minutes after the galvanostatic charging at various potentials. (b) Gravimetric discharge capacities at 0.1, 0.4 and 1.6 A g^{-1} current densities of the OMIECs when charged to |1.2| V. The 10th cycle of the galvanostatic charging/discharging curves was used for the calculations. (c) Schematic of an all-OMIEC full cell operated with an ionic liquid electrolyte. (d) Discharge capacity of p($g_3C_2T_2$-T):PBFDO full cell over 150 cycles at 0.1 A g^{-1} current density when cycled to 2.4 V.

p(g_3C_2T2-T) and PBFDO are the only materials that maintained voltage losses below 10% throughout the tested potential range. Note that ±1.2 V was chosen as the maximum operational potential for individual electrodes, based on the electrochemical stability range of EMIM:TFSI, which is ±2 V.[19] Therefore, when the cathode and anode are paired and each is charged to its respective maximum potential, the full cell achieves an operating voltage of approximately 1.4 V.

Next, we evaluated the gravimetric capacities of the anodes and the cathode in half-cell configurations across various current densities to identify the best-performing OMIEC (Fig. 4b). The galvanostatic charging/discharging curves used for these calculations are shown in Fig. S9–S11.† PBFDO emerged as the top performer at low current densities, exhibiting a gravimetric capacity of 110 mA h g^{-1} at 0.1 A g^{-1} and 65 mA h g^{-1} at 0.4 A g^{-1}, highlighting its potential for battery applications. However, PBFDO's capacity declines at higher current densities (*e.g.* 1.6 A g^{-1}), in contrast to recent results reported by Ohayon *et al.*,[4] where PBFDO demonstrated high capacities even at rates exceeding 10 A g^{-1} when used in a capacitor configuration. We hypothesize that this discrepancy arises from the use of high-viscosity ionic liquid molded into a solid gel matrix in our device. While this architecture allows for a solid-state device with an effective O_2/H_2O barrier, it may restrict ionic mobility and charge transport at high rates.

Since both PBFDO and p(g_3C_2T2-T) exhibit low thermally driven self-discharge and maintain high, comparable gravimetric capacities across all charging rates, we expect high charging/discharging efficiency and minimized risks of overcharging or undercharging in the full-cell configuration. Consequently, we selected PBFDO as the anode to pair with the p(g_3C_2T2-T) cathode for full-cell performance testing, using equal mass loadings. During charging, $EMIM^+$ cations migrate toward the anode (PFBDO), and $TFSI^-$ anions move toward the cathode (p($g_3C_2T_2$-T)) (Fig. 4c), penetrating the OMIECs due to the polymers' volumetric ion uptake capability. This process is driven by the reduction of the cathode and oxidation of the anode through an external current or voltage source—in this case, a potentiostat. During discharge, the cell is connected to a load, the stored electrochemical energy is released from the cell as the anode is oxidized and the cathode is reduced, returning each electrode to its baseline state. We exposed the

PBFDO-p(g_3C_2T2-T) full-cell to 150 galvanostatic charge–discharge cycles at 0.1 A g^{-1} (Fig. 4d), achieving a maximum cell voltage of 2.4 V. The discharge capacity was 25.73 mA h g^{-1} in the first cycle; by the 145th cycle, the capacity had dropped by approximately 12% to 22.62 mA h g^{-1}. In the first five cycles, the coulombic efficiency was low, starting at 63.65% and but increased to 98.45% by the 5th cycle, indicating a five-cycle burn-in requirement. For the remaining cycles, the device maintained an average coulombic efficiency of 97.3%. However, after the 145th cycle, there was a drastic drop in capacity, falling to 14.6 mA h g^{-1} by the 150th cycle. Thanks to our cell design, which includes an embedded reference electrode enabling a three-electrode diagnostics of the half cell, we were able to pinpoint the source of failure. Post-mortem analysis revealed that the cathode was no longer able to generate current, while the anode remained functional. This suggests a mechanical failure, likely due to the delamination of the p-type film or the lost connection between the carbon paper and gold-coated glass (Fig. S12†).

We also evaluated the rate capability of this full cell (Fig. 5a) across a range of current densities, from 0.05 A g^{-1} to 1.6 A g^{-1}, followed by a return to 0.05 A g^{-1}. After five cycles at each current density, we observed a ~30% reduction in gravimetric capacity upon returning to 0.05 A g^{-1} relative to the initial capacity at that density. For 0.1 A g^{-1} and for 0.2 A g^{-1}, the capacity losses were around 20% and 9.8%, respectively. These reductions, particularly at lower current densities, likely reflect the cell's burn-in phase - also evident in the long-term cycling data (Fig. 4d), where the gravimetric capacity stabilizes over time. Throughout all return cycles, the coulombic efficiency remained between 96% and 100%, except at the high rate of 1.6 A g^{-1}, where a decline in efficiency was observed. These findings are consistent with our half-cell evaluations, in which PBFDO displayed reduced performance at higher charging rates (Fig. 4b). Raw galvanostatic charge–discharge data for the 5th cycle at each current density are provided in Fig. S13.† To contextualize the device's performance, we constructed a Ragone plot, comparing the energy *vs.* power density of our full cell against previously reported OMIEC-based charge storage devices (Fig. 5b). While a recently reported symmetric cell using PBFDO achieved a higher power density,[4] our cell stands out for its higher energy density, approaching that of battery-like devices. This enhancement is attributed to the cell's high operating voltage of 2.4 V, enabled by the broad electrochemical stability window of the ionic liquid electrolyte[19] and the robust device architecture incorporating an effective O_2/H_2O barrier.

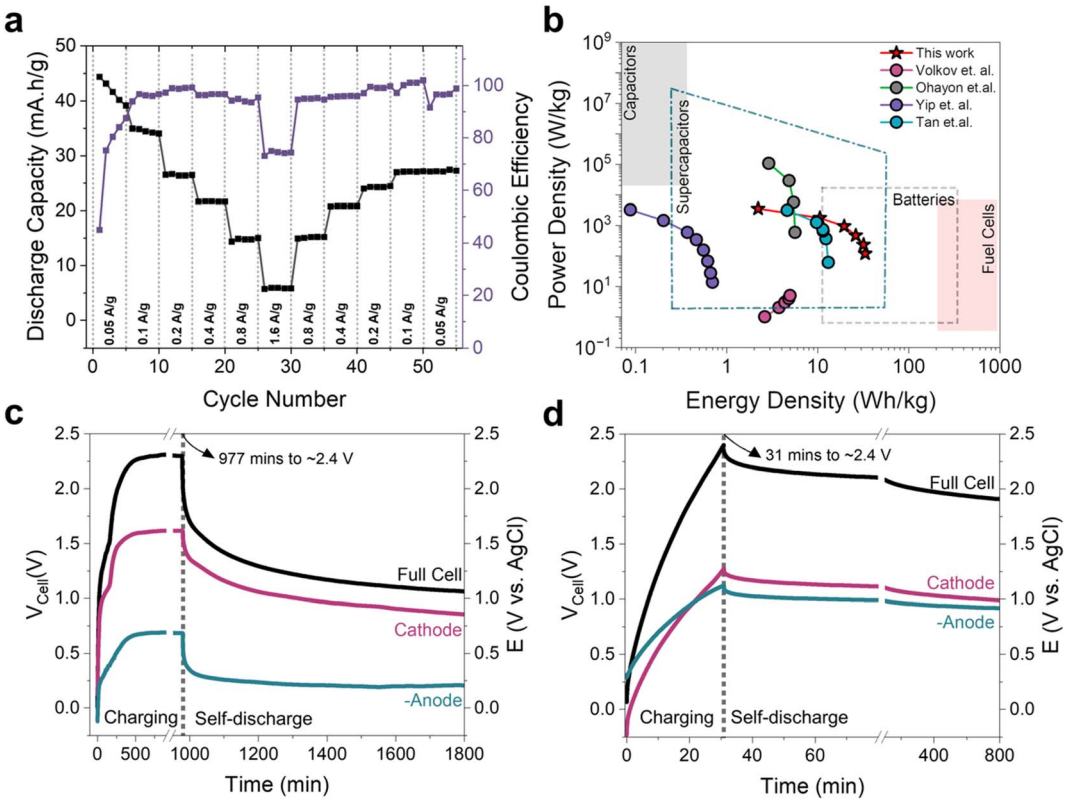

Fig. 5 (a) Charge–discharge capacity of p($g_3C_2T_2$-T):PBFDO full cell at different gravimetric current densities *vs.* cycle number when cycled to 2.4 V. (b) Ragone plot showing the performance of p($g_3C_2T_2$-T):PBFDO full cell compared to other similar OMIEC based charge storage devices (ref. 1, 4, 32 and 47). Power and energy densities were calculated with respect to the total active material weight. Charging of the p($g_3C_2T_2$-T):PBFDO full cells at 0.1 A g^{-1} and subsequent self-discharge when the cells are fabricated (c) without barrier and (d) with barrier. The full cell potential is shown on the left axis, while cathode and anode potentials are shown on the right, recorded using the lateral pseudo reference electrode.

The importance of the O_2/H_2O barrier is further underscored by the discharge experiments shown in Fig. 5c and d. When the full cell is charged at 0.1 A g^{-1} in ambient conditions without a barrier it fails to reach the target voltage of 2.4 V, even after *ca.* 16 hours of continuous charging (Fig. 5c). Probing the cell using a pseudo-reference electrode reveals that, while the cathode reaches 1.7 V, the anode only reaches −0.7 V. This results in overcharging of the cathode and undercharging of the anode, deviating from the expected symmmetric polarization at ±1.2 V . In an efficient all-OMIEC device with similar mass loading (0.1 mg for both electrodes in our case), achieving equal polarization on the cathode and anode is crucial to avoid such voltage mismatches. We speculate that the undercharging of the PBFDO anode is due to the continuous ORR, which prevents proper anode polarization and, in turn, drives overdrive the cathode.[48] In contrast, Fig. 5d shows that when a barrier is applied, the full cell reaches 2.4 V within 30 minutes at the same current density, with the cathode and anode reaching ∼1.25 V and −1.15 V, respectively. Comparing self-discharge between the two cases further illustrates the impact of the barrier: the barrier-free cell loses 1 V at the cathode and 0.6 V at the anode (a 75% total loss) after 700 minutes, while the encapsulated cell shows a much lower full-cell loss of just 0.5 V (0.3 V at the cathode and 0.2 V at the anode) over the same period. These results clearly highlight the essential role of the barrier in preserving voltage and enabling reliable performance in OMIEC-based charge storage systems. Moreover, they demonstrate the diagnostic value of the pseudo-reference electrode in identifying performance-limiting phenomena. Additionally, to emphasize the uniqueness of the barrier used in this study, we tested a commercially available two-part epoxy glue as an alternative sealing material. As shown in Fig. S15†, the epoxy-sealed cell failed to reach 2.4 V even after 3000 minutes of charging, performing similar to a barrier-free cell. Unlike generic epoxy glue, our barrier serves more than just an adhesive—it creates a fully enclosed, localized, glove box-like environment for the electrodes and gel (Fig. 3). By effectively restricting O_2 and H_2O from reaching the electrodes, the barrier eliminates the need for a closed system operation, enables ambient operation without sacrificing performance and significantly advances the practicality of OMIEC-based charge storage devices for scalable, real-world applications.

Conclusions

In this work, we leveraged the wide electrochemical operating range of ionic liquids and their compatibility with polymeric gels to develop organic mixed ionic-electronic conductor (OMIEC)-based charge storage devices. The cells employed a solid electrolyte gel composed of the ionic liquid EMIM-TFSI embedded in a PEO matrix. Compared to the conventionally used PVDF-HFP, PEO demonstrated superior film-forming performance and adhesion to OMIEC surfaces, making it a more suitable matrix for charge storage applications. The gel electrolyte also enabled encapsulation of the device with an O_2 and H_2O barrier, preventing Faradaic self-discharge reactions and ensuring air stability. To enable electrochemical analysis, we incorporated a pseudo-reference electrode into the device architecture. This allowed simultanous evaluation of both half-cell and full-cell behavior within a single platform, facilitating independent assessment of the cathode and anode dynamics during full-cell operation. For example, using this setup, we observed that Faradaic reactions limited the charging potential of the anode, resulting in anode undercharging and cathode overcharging in the absence of a barrier. In addition to gravimetric capacity, we also evaluated the thermal self-discharge levels of OMIECs to identify the optimal cathode–anode pairing for full-cell performance. Based on these assessments, we selected p(g_3C_2T2-T):PBFDO pair as the optimal cathode–anode combination. Full-cell tests revealed a short burn-in period of approximately 10 cycles, after which gravimetric capacity stabilized around 25 mA h g^{-1}. The device supported operation up to 2.4 V and achieved energy densities exceeding 115 W h kg^{-1}—surpassing all previously reported OMIEC-based charge storage systems. Our findings demonstrate that the combination of gel electrolytes, engineered environmental barriers, and integrated diagnostics could significantly enhance the performance and stability of OMIEC-based charge storage devices. Given their metal-free, environmentally abundant composition and tunable properties, OMIECs hold strong promise for next-generation sustainable charge storage technologies, especially when designed with application-specific performance metrics in mind.

Methods

Materials

BBL (N41A50) was purchased from n-ink AB Sweden and was used after 10 min of sonication in a bath sonicator. EMIM TFSI, PEO (M_w ∼4 000 000 g mol^{-1}), chloroform, acetone, and acetonitrile were purchased from Sigma Aldrich and were used as is. FLEXGLOO-U1/SEU10 as water barrier and FLEXGLOO-O2/SEU10 as oxygen barrier were procured from SAES Getters S.p.A. Italy and were used according to the instructions provided by the manufacturer. Elcocarb B-L/SP carbon paste was purchased from Solaronix Switzerland and was used as is. Conducting silver paste was procured from Merck, Chlorox was bought from the local supermarket, and Toray Carbon Paper TGP-H-060 was procured from Fuel cell store. P-90,[10] p(C_6-NDI-T),[30,42] PBFDO[33,34,48] and p(g_3C_2T2-T)[42] were synthesized using existing protocols.

Electrode preparation

Gold electrodes were prepared using standard photolithography procedures. Briefly, 4-inch glass wafers were cleaned in piranha solution before coating with the photoresist and subsequently exposed using a custom photomask. Metal interconnects were deposited using magnetron sputtering of chromium, acting as an adhesion layer, followed by gold. Lift-off was achieved using appropriate solvents. Our insulation layer was deposited using chemical vapor deposition of Parylene-C. A thick photoresist layer was deposited, baked, and patterned before revealing the openings for semiconductor patterning. Lastly, the patterns

were opened using reactive-ion plasma etching. The electrodes were cut from the wafer using a diamond cutter before use. Carbon paper was cut into 10 × 5 mm rectangles and pasted on the fabricated Au electrodes using the carbon paste and annealed at 100 °C. P-90, p(C_6-NDI-T), and p(g_3C_2T2-T) solutions were prepared in chloroform (5 mg mL^{-1}) by heating at 60 °C for 30 minutes. 0.1 mg of these solutions were drop cast on the carbon electrodes and left to dry in air for 30 minutes before use. For PBFDO, the required amount of polymer solution in DMSO was drop cast on the electrode and was left to dry in a vacuum chamber at 90 °C for 2 hours. One of the carbon electrodes was left uncovered and used as a counter electrode. The reference electrode was prepared by depositing a drop of silver paste on the gold electrodes. After curing the silver paste, this area was covered by a drop of Chlorox for 12 hours. The Clorox was washed off using DI water. The reference electrode was evaluated extensively for stability and referenced against a true Ag/AgCl reference electrode (see Section 1 of ESI†).

Electrolyte preparation

EMIM-TFSI:PVDF-HFP based electrolyte was prepared by simultaneously dissolving p(VDF-HFP) and EMIM-TFSI in acetone. The proportions by weight of the polymer, ionic liquid, and solvent were maintained at 1 : 4 : 7, respectively. EMIM-TFSI:PEO based electrolyte was prepared by dissolving PEO in acetonitrile at a concentration of 25 mg mL^{-1} to make a stock solution. 248 mg of EMIM-TFSI was added to every 1 g of the PEO-Acetonitrile mixture. This mixture ensured that the ionic liquid and PEO were in an 8 : 1 mass ratio once acetonitrile had evaporated.

Preparation of the electrochemical cell

The cathode, anode, counter, and reference electrodes were fixed on a glass slide using a super glue. These cells were transferred to the glove box, where the electrolyte was deposited using a pasture pipette to cover all the electrodes. After the electrolyte dried, a second layer of electrolyte was deposited and left to dry to ensure coverage. Finally, a small piece of glass slide was pressed over the active electrode area to ensure no disturbance to the gel electrolyte.

Preparation of the O_2/H_2O barrier

We used a combination of commercially available O_2 and H_2O barriers, typically used to encapsulate organic light-emitting diodes, to shield cells from parasitic discharging and degradation. These barriers fill the air gap between the two glass slides above the electrolyte and below the electrodes. The H_2O barrier, FlexGloo-U1, was first filled into this gap using a syringe. Areas where the electrode active area was visible on the cell were covered with aluminum tape before the barrier was cross-linked using UV light for 30 minutes to avoid degradation of the OMIECs. The O_2 barrier, FLEXGLOO-O2/SEU10, was then deposited similarly, but the crosslinking was done using thermal annealing of the film at 100 °C for 30 min. The product booklet for the barrier product range can be found here: **https://saes-usa.com/Flyeredits/FlexGloo/FlexGloo.pdf**.

Electrochemical evaluation

A VSP-300 biologic potentiostat/galvanostat was employed to record cyclic voltammograms of the films, as well as device and electrode responses, using chronoamperometry, chronopotentiometry, and open circuit voltage measurements. These experiments utilized a lateral AgCl pseudo-reference electrode and a carbon paper counter electrode. For half-cell evaluations, a traditional three-electrode setup was used, with the evaluated electrode as the working electrode. In full-cell evaluations, the working electrode was connected to the cathode, while the counter electrode, shorted to the reference electrode, was connected to the anode. An additional channel recorded the electrochemical potential of the cathode using the on-device AgCl pseudo-reference electrode, with the working electrode connected to the cell's cathode. All full cell and half cell evaluations were performed with a barriered cell unless mentioned otherwise.

The formula used for energy density is:

$$\text{Energy density} = \frac{1}{\text{total mass}} \cdot \int_{t=0}^{t=\text{charged}} I \cdot E_{\text{Cell}}(t) \cdot \mathrm{d}t$$

and for power density is:

$$\text{Power density} = \frac{1}{\text{total mass}} \cdot I \cdot E_{\text{Cell}}$$

where I is the galvanostatic charging/discharging current, $E_{\text{Cell}}(t)$ is the cell voltage with respect to time and t is the time.[1]

In situ UV-vis measurements

We prepared a cell as shown in Fig. 1a with the exception that the working and counter electrodes were prepared on ITO to ensure light transmission. Measurements were performed using an Ocean Optics HL-2000-FHSA halogen light source and Ocean Optics QE65 Pro Spectrometer. The light was guided through a fiber-optic cable to the polymer film inside the electrochemical cell. The OceanView software was first calibrated using the counter electrode covered by the gel electrolyte. The OMEIC films were biased using a Biologic SP-300 using cyclic voltammetry while recording the UV-vis spectra.

Data availability

The authors declare that the data supporting the findings of this study are available within the paper and its ESI files.† Should any raw data files be needed in another format, they are available from the corresponding author upon request.

Author contributions

P. D. N. conceived the research, designed the experiments and methodology, performed the electrochemical measurements, analyzed the data, and wrote the manuscript. D. O., L. S., and T. C. H. C helped with the experimental design and manuscript draft. A. H. and S. B. fabricated some of the electrodes. D.A. performed additional electrochemical measurements. R.S. synthesized the p(C_6-NDI-T) and p(g_3C_2T2-T), supervised by

I. M. H. T. synthesized the PBFDO supervised by F. H. S. I. conceptualized and supervised the work, designed the experiments, and wrote the manuscript. All authors were involved in the discussion and participated in manuscript input.

Conflicts of interest

There are no conflicts to declare.

Acknowledgements

This publication is based upon work supported by the King Abdullah University of Science and Technology (KAUST) under Award No. OSR-2019-CRG8-4095, OSR-2019-CRG10-4668, and ORA-2021-CRG10-4650.

References

1 S. T. M. Tan, T. J. Quill, M. Moser, G. Lecroy, X. Chen, Y. Wu, C. J. Takacs, A. Salleo and A. Giovannitti, *ACS Energy Lett.*, 2021, **6**, 3450–3457.
2 T. Ma, Y. Yang, D. Johnson, K. Hansen, S. Xiang, R. M. Thakur, A. Djire and J. L. Lutkenhaus, *Joule*, 2023, **7**, 2261–2273.
3 J. Bitenc, K. Pirnat, O. Lužanin and R. Dominko, *Chem. Mater.*, 2024, **36**, 1025–1040.
4 D. Ohayon, G. Quek, B. R. P. Yip, F. Lopez-Garcia, P. R. Ng, R. J. Vázquez, D. V. Andreeva, X. Wang and G. C. Bazan, *Adv. Mater.*, 2024, **36**(47), 2410512.
5 G. Nikiforidis, S. Wustoni, D. Ohayon, V. Druet and S. Inal, *ACS Appl. Energy Mater.*, 2020, **3**, 7896–7907.
6 B. Esser, F. Dolhem, M. Becuwe, P. Poizot, A. Vlad and D. Brandell, *J. Power Sources*, 2021, **482**, 228814.
7 A. Gandini and T. M. Lacerda, *Prog. Polym. Sci.*, 2015, **48**, 1–39.
8 B. D. Paulsen, S. Fabiano and J. Rivnay, *Annu. Rev. Mater. Res.*, 2021, **51**, 1–27.
9 Y. Wang, S. Wustoni, J. Surgailis, Y. Zhong, A. Koklu and S. Inal, *Nat. Res.*, 2024, **9**, 249–265.
10 A. Giovannitti, I. P. Maria, D. Hanifi, M. J. Donahue, D. Bryant, K. J. Barth, B. E. Makdah, A. Savva, D. Moia, M. Zetek, P. R. F. Barnes, O. G. Reid, S. Inal, G. Rumbles, G. G. Malliaras, J. Nelson, J. Rivnay and I. McCulloch, *Chem. Mater.*, 2018, **30**, 2945–2953.
11 D. H. L. Tjhe, X. Ren, I. E. Jacobs, G. D'Avino, T. B. E. Mustafa, T. G. Marsh, L. Zhang, Y. Fu, A. E. Mansour, A. Opitz, Y. Huang, W. Zhu, A. H. Unal, S. Hoek, V. Lemaur, C. Quarti, Q. He, J. K. Lee, I. McCulloch, M. Heeney, N. Koch, C. P. Grey, D. Beljonne, S. Fratini and H. Sirringhaus, *Nat. Mater.*, 2024, **23**, 1712–1719.
12 S. T. M. Tan, A. Gumyusenge, T. J. Quill, G. S. LeCroy, G. E. Bonacchini, I. Denti and A. Salleo, *Adv. Mater.*, 2022, **34**(21), 2110406.
13 D. Moia, A. Giovannitti, A. A. Szumska, I. P. Maria, E. Rezasoltani, M. Sachs, M. Schnurr, P. R. F. Barnes, I. McCulloch and J. Nelson, *Energy Environ. Sci.*, 2019, **12**, 1349–1357.
14 J. Bai, D. Liu, X. Tian and S. Zhang, *J. Mater. Chem. C*, 2022, **10**, 13303–13311.
15 N. Li, Y. Li, Z. Cheng, Y. Liu, Y. Dai, S. Kang, S. Li, N. Shan, S. Wai, A. Ziaja, Y. Wang, J. Strzalka, W. Liu, C. Zhang, X. Gu, J. A. Hubbell, B. Tian and S. Wang, *Science*, 2023, **381**, 686–693.
16 Y. Dai, S. Dai, N. Li, Y. Li, M. Moser, J. Strzalka, A. Prominski, Y. Liu, Q. Zhang, S. Li, H. Hu, W. Liu, S. Chatterji, P. Cheng, B. Tian, I. McCulloch, J. Xu and S. Wang, *Adv. Mater.*, 2022, **34**(23), 2201178.
17 X. Li, Y. Li, K. Sarang, J. Lutkenhaus and R. Verduzco, *Adv. Funct. Mater.*, 2021, 1–7.
18 K. H. Lee, M. S. Kang, S. Zhang, Y. Gu, T. P. Lodge and C. D. Frisbie, *Adv. Mater.*, 2012, **24**, 4457–4462.
19 M. Hayyan, F. S. Mjalli, M. A. Hashim, I. M. AlNashef and T. X. Mei, *J. Ind. Eng. Chem.*, 2013, **19**, 106–112.
20 J. Surgailis, P. D. Nayak, L. Q. Flagg, C. J. Kousseff, I. McCulloch, L. J. Richter and S. Inal, *Mater. Sci. Eng., R*, 2025, **163**, DOI: 10.1016/j.mser.2025.100944.
21 M. Armand, F. Endres, D. R. MacFarlane, H. Ohno and B. Scrosati, *Nat. Mater.*, 2009, **8**, 621–629.
22 Y. Zhong, N. Lopez-Larrea, M. Alvarez-Tirado, N. Casado, A. Koklu, A. Marks, M. Moser, I. McCulloch, D. Mecerreyes and S. Inal, *Chem. Mater.*, 2024, **36**, 1841–1854.
23 R. Yuan, Y. Dong, R. Hou, S. Zhang and H. Song, *J. Electrochem. Soc.*, 2022, **169**, 030504.
24 A. De La Fuente Durán, A. Y. L. Liang, I. Denti, H. Yu, D. Pearce, A. Marks, E. Penn, J. Treiber, K. Weaver, L. Turaski, I. P. Maria, S. Griggs, X. Chen, A. Salleo, W. C. Chueh, J. Nelson, A. Giovannitti and J. T. Mefford, *Energy Environ. Sci.*, 2023, **16**, 5409–5422.
25 M. Vagin, V. Gueskine, E. Mitraka, S. Wang, A. Singh, I. Zozoulenko, M. Berggren, S. Fabiano and X. Crispin, *Adv. Energy Mater.*, 2021, **11**, 1–8.
26 V. Druet, P. D. Nayak, A. Koklu, D. Ohayon, A. Hama, X. Chen, M. Moser, I. McCulloch and S. Inal, *Adv. Electron. Mater.*, 2022, **8**(10), 2200065.
27 Y. Zhang, E. R. W. van Doremaele, G. Ye, T. Stevens, J. Song, R. C. Chiechi and Y. van de Burgt, *Adv. Mater.*, 2022, **34**(20), 2200393.
28 A. Giovannitti, I. P. Maria, D. Hanifi, M. J. Donahue, D. Bryant, K. J. Barth, B. E. Makdah, A. Savva, D. Moia, M. Zetek, P. R. F. Barnes, O. G. Reid, S. Inal, G. Rumbles, G. G. Malliaras, J. Nelson, J. Rivnay and I. McCulloch, *Chem. Mater.*, 2018, **30**, 2945–2953.
29 A. Koklu, D. Ohayon, S. Wustoni, A. Hama, X. Chen, I. McCulloch and S. Inal, *Sens. Actuators, B*, 2021, **329**, 129251.
30 A. Koklu, S. Wustoni, V. E. Musteata, D. Ohayon, M. Moser, I. McCulloch, S. P. Nunes and S. Inal, *ACS Nano*, 2021, **15**, 8130–8141.
31 C. Y. Yang, M. A. Stoeckel, T. P. Ruoko, H. Y. Wu, X. Liu, N. B. Kolhe, Z. Wu, Y. Puttisong, C. Musumeci, M. Massetti, H. Sun, K. Xu, D. Tu, W. M. Chen, H. Y. Woo,

M. Fahlman, S. A. Jenekhe, M. Berggren and S. Fabiano, *Nat. Commun.*, 2021, **12**, 2354.
32 A. V. Volkov, H. Sun, R. Kroon, T. P. Ruoko, C. Che, J. Edberg, C. Müller, S. Fabiano and X. Crispin, *ACS Appl. Energy Mater.*, 2019, **2**, 5350–5355.
33 H. Tang, Y. Liang, C. Liu, Z. Hu, Y. Deng, H. Guo, Z. Yu, A. Song, H. Zhao, D. Zhao, Y. Zhang, X. Guo, J. Pei, Y. Ma, Y. Cao and F. Huang, *Nature*, 2022, **611**, 271–277.
34 J. C. Flores, P. Hayoz, I. McCulloch, N. Onwubiko, D. Kaelblein, W. Yue, H. Y. Chen and A. C. Knall, *Semiconducting polymer*, US10815236B2, 2017.
35 F. Huang and H. Tang, *A kind of n-type conjugated polymer blend and its preparation method and application*, WO2023056662A1, 2023.
36 A. Koklu, S. Wustoni, K. Guo, R. Silva, L. Salvigni, A. Hama, E. Diaz-Galicia, M. Moser, A. Marks, I. McCulloch, R. Grünberg, S. T. Arold and S. Inal, *Adv. Mater.*, 2022, **34**(35), 2202972.
37 T. J. Quill, G. LeCroy, A. Melianas, D. Rawlings, Q. Thiburce, R. Sheelamanthula, C. Cheng, Y. Tuchman, S. T. Keene, I. McCulloch, R. A. Segalman, M. L. Chabinyc and A. Salleo, *Adv. Funct. Mater.*, 2021, **31**(47), 2104301.
38 T. J. Quill, G. LeCroy, D. M. Halat, R. Sheelamanthula, A. Marks, L. S. Grundy, I. McCulloch, J. A. Reimer, N. P. Balsara, A. Giovannitti, A. Salleo and C. J. Takacs, *Nat. Mater.*, 2023, **22**, 362–368.
39 A. Melianas, T. J. Quill, G. LeCroy, Y. Tuchman, H. v. Loo, S. T. Keene, A. Giovannitti, H. R. Lee, I. P. Maria, I. McCulloch and A. Salleo, *Sci. Adv.*, 2020, **6**, 27.
40 J. O. Guardado and A. Salleo, *Adv. Funct. Mater.*, 2017, **27**(32), 1701791.
41 Y. Zhong, P. D. Nayak, S. Wustoni, J. Surgailis, J. Z. Parrado Agudelo, A. Marks, I. McCulloch and S. Inal, *Am. Chem. Soc.*, 2024, **16**(45), 61457–61466.
42 A. Koklu, S. Wustoni, K. Guo, R. Silva, L. Salvigni, A. Hama, E. Diaz-Galicia, M. Moser, A. Marks, I. McCulloch, R. Grünberg, S. T. Arold and S. Inal, *Adv. Mater.*, 2022, **34**, 1–12.
43 A. Khan, X. Lu, L. Aldous and C. Zhao, *J. Phys. Chem. C*, 2013, **117**, 18334–18342.
44 Y. Zhang and C. Pozo-Gonzalo, *Chem. Commun.*, 2018, **54**, 3800–3810.
45 D. Alwast, J. Schnaidt, Z. Jusys and R. J. Behm, *J. Electrochem. Soc.*, 2020, **167**, 070505.
46 B. Babu, *Energy Storage Mater.*, 2024, **67**, 103261.
47 B. R. P. Yip, R. Javier Vázquez, Y. Jiang, S. R. McCuskey, G. Quek, D. Ohayon, X. Wang and G. C. Bazan, *Adv. Mater.*, 2024, **36**(1), 2308631.
48 X. Wu, H. Tang, Z. Zhou, T. Salim, C. G. Tang, F. Huang and W. L. Leong, *Chem. Mater.*, 2024, **36**(18), 8639–8648.